Soft Matter

PAPER

View Article Online
View Journal | View Issue

Cite this: *Soft Matter*, 2024, **20**, 2777

Dynamics of self-propelled particles in vibrated dense granular media†

Kyungmin Son,[a] Yunsik Choe,[b] Euijoon Kwon,[b] Leonardo Garibaldi Rigon,[b] Yongjoo Baek*[b] and Ho-Young Kim*[ac]

Received 24th November 2023,
Accepted 27th February 2024

DOI: 10.1039/d3sm01596c

rsc.li/soft-matter-journal

We study a system consisting of a few self-propelled particles (SPPs) placed among a crowd of densely packed granular particles that are vertically vibrated in a two-dimensional circular confinement. Our experiments reveal two important findings. First, an SPP exhibits a fractal renewal process within the dense granular medium, which induces a superdiffusive behavior whose diffusion exponent increases with its aspect ratio. Second, the SPPs eventually reach the boundary and form a moving cluster, which transitions from the moving state to the static state as the number of SPPs is increased. These results suggest a simple and effective method of modulating the fluidity and directionality of granular systems *via* controlling the shape and the number of SPPs.

I. Introduction

Various systems in nature exhibit self-organization, where complex structures emerge from simple interactions among individual elements without any centralized control.[1] This has inspired the development of "swarm robotics", which aims to design artificial systems whose milli-scale or larger components self-organize into a predetermined target structured through reprogrammable interactions.[2–8] However, these approaches are based on components that only engage in weak mutual interactions, prioritizing a flexible structure at the cost of making it robust against external stress. Interestingly, many naturally occurring self-organized structures manage to maintain their overall shape, even as they remain flexible enough to carry out diverse functions. This is exemplified by various proteins that sit almost exactly at the rigidity transition in their native state.[9,10] In this regard, the issue of reprogrammable self-organization still faces a core challenge: one must find a balance between structural stability, which demands solid-like rigidity, and structural flexibility, which requires the components to rearrange themselves in a fluid-like manner.

Active granular media, comprised of polar particles that effectively self-propel on a vibrated surface, present a promising approach to this challenge. Neither fully solid-like nor liquid-like, granular materials generally exhibit a variety of mechanical properties depending on the physical situation.[11–14] In particular, a two-dimensional (2D) layer of vibrated granular medium can be made to form both solid and liquid-like phases by tuning the vibration amplitude.[15] Moreover, when such medium consists of self-propelled particles (SPPs), it exhibits a rich range of collective phenomena including flocking,[16–18] clogging,[19–21] crystallization,[22] and phase separation.[23,24] It should be noted that even a small fraction of SPPs mixed with the ordinary granular particles can dramatically alter the properties of the system, as exemplified by the promotion of crystallization,[25,26] the acceleration of domain coarsening,[27] and the generation of global nonequilibrium flux *via* positive feedback between the flocking of SPPs and the rectified currents of granular particles.[28,29] Those motivate us to look into the physics of a granular medium with a small number of SPPs, which can be regarded as "active dopants" whose geometric and mechanical features can be adjusted to change the structure and function of the whole system.

In this study, as a minimal empirical representation of the granular media with active dopants, we study the dynamics of SPPs placed among a dense crowd of vibrated granular particles in a 2D circular confinement. Previous research has touched upon such systems in light of global ordering[28,29] and microscopic fluctuations.[30] However, the motion of an individual SPP within the granular medium, the emergent order when there are only a handful of SPPs within the system, and the effects of the shape of each SPP on these phenomena remain underexplored.

Our investigation reveals two distinct phenomena: first, the traversal of an SPP to the confinement boundary through a "fractal renewal process",[31] characterized by a power-law waiting time distribution influenced by the shape of the SPP. Second,

[a] *Department of Mechanical Engineering, Seoul National University, Seoul 08826, Korea. E-mail: hyk@snu.ac.kr*
[b] *Department of Physics and Astronomy & Center for Theoretical Physics, Seoul National University, Seoul 08826, Korea. E-mail: y.baek@snu.ac.kr*
[c] *Institute of Advanced Machines and Design, Seoul National University, Seoul 08826, Korea*

† Electronic supplementary information (ESI) available. See DOI: https://doi.org/10.1039/d3sm01596c

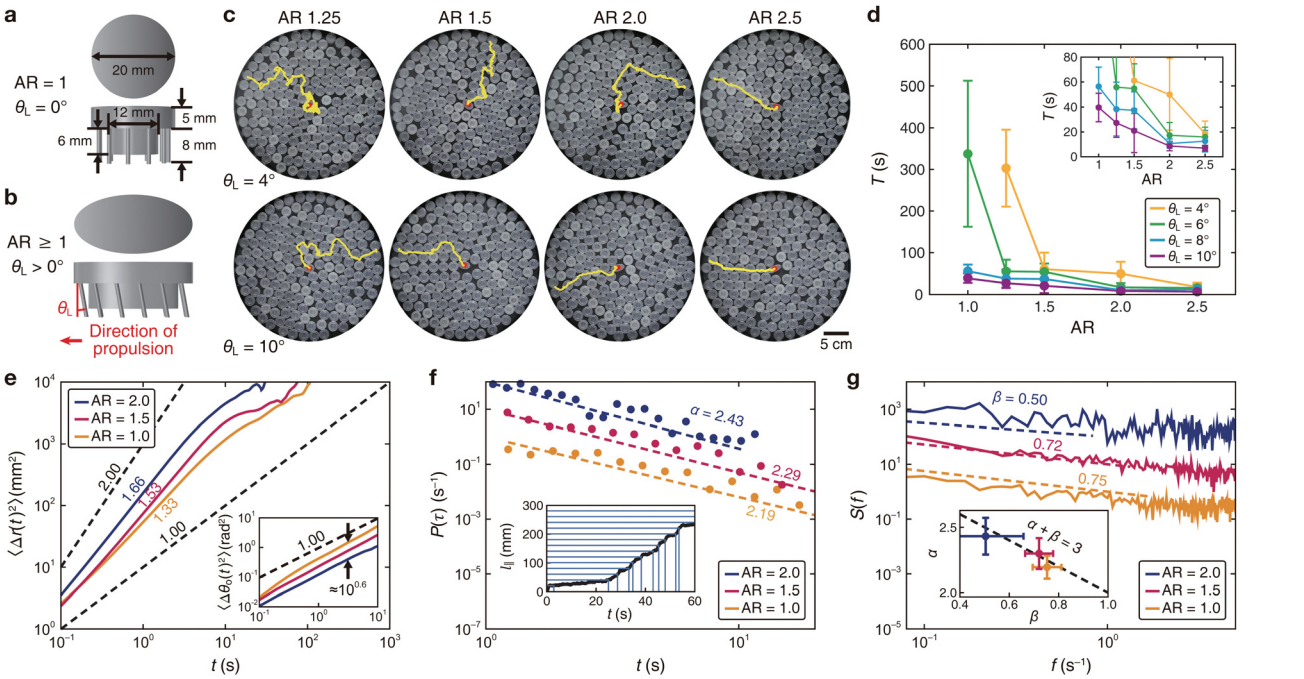

Fig. 1 Dynamics of a single SPP placed in the center of densely packed isotropic particles. (a) Top and side views of a circular isotropic particle. (b) Top and side views of an elliptic SPP. Thicknesses of the disks and leg length are the same as the isotropic particle. (c) Trajectories of a single SPP as the leg tilt angle θ_L and the aspect ratio (AR) are varied (Movie S1, ESI†). (d) Time to reach the boundary, T, as θ_L and AR are varied. Error bars indicate standard deviation. (e) Time-averaged mean squared displacement of the SPP. (inset) Time-averaged mean squared angular displacement of the same SPP. (f) Interevent time probability $P(\tau) \sim \tau^{-\alpha}$ characterizing the axial motion of the SPP at $\theta_L = 10°$. (inset) Example of the time evolution of the axial displacement for AR = 1.0. (g) Power spectrum $S(f) \sim f^{-\beta}$ of the axial velocity of the SPP. (inset) Power-law exponents α and β are consistent with the relation $\alpha + \beta = 3$ up to error bars.

when the number of SPPs is small enough, a single motile cluster forms at the boundary, exhibiting persistent unidirectional movement due to a positive feedback loop between the cluster's asymmetry and its motion. The underlying mechanism is reminiscent of the spontaneous symmetry-breaking motility involving active fluids.[32–39] The phenomenon occurs even when the confinement boundary is simply circular, a setup that has been avoided in the previous research[16–18,28,29] that employed a petal-shaped confinement instead to inhibit the boundary aggregation of SPPs.[40] These results open up new avenues for controlling the fluidity and directionality of granular systems using a limited number of SPPs.

II. Experimental setup

A. Particle fabrication

As shown in Fig. 1a and b, each particle consists of two elliptic cylinders, the cap (height 5 mm) and the body (height 6 mm), joined on the same axis. For a circular particle, the diameters of the cap and the body are 20 mm and 12 mm, respectively, while the cap and the body of an elliptic particle have the same area, height, and mass as the corresponding parts of the circular particle. Eleven legs (length 8 mm, diameter 1 mm) are attached to the cap, which are tilted from the vertical direction by the identical angle less than 10°. All particles are manufactured by stereolithography 3D printing (Formlabs Form 3) using acrylate-based clear photopolymer. The geometric accuracy of the 3D printer employed in this work is approximately ±0.1 mm. For robust tracking of the position and the orientation of particles of interest, we mark them with one or two red squares at the top. Then the TrackMate plug-in for ImageJ[41] is used to trace and analyze the trajectories.

B. Vibrating table

The SPPs and the circular particles are excited by vertical vibration of the circular acrylic baseplate (diameter 350 mm, height 30 mm) attached to an electromagnetic shaker (Tira TV 5220). The plate is kept horizontal with an accuracy of 0.1°. Particle motion is restricted by an enclosing ring (diameter 300 mm). The shaker is attached to heavy concrete blocks to suppress resonances. Experiments are performed with vibrations at frequency $f = 80$ Hz and amplitude $A = 70$ μm, which guarantees stable excitation of particles.

III. Motion of a single self-propelled particle

A. Experimental observations

We first observe how a single SPP moves amidst a crowd of vibrating granular particles. For this purpose, we placed a 2D circular confinement horizontally upon a vertically vibrating plate, with legged particles filling 75% of its area (170 particles

in total). All but one of the particles (Fig. 1a) have a circular top and vertical legs, which move around randomly in an unbiased manner on the vibrating plate. In addition to these isotropic particles, there is a single particle whose legs are tilted from the vertical direction along the major axis of its elliptic top (Fig. 1b). Collisions of these tilted legs with the vibrating plate result in a fluctuating horizontal force that propels the particle in the direction indicated in Fig. 1b. Thus, this particle becomes an SPP exhibiting directed motion. The physical properties of the SPP can be controlled by varying the leg title angle θ_L and the aspect ratio (AR) of the elliptic top while maintaining its total area equal to that of an isotropic particle. In the absence of other particles, the axial velocity of the SPP increases with θ_L but does not vary significantly with the AR (see Fig. 5).

The SPP is initially put at the center of the circular confinement. When the vibration is turned on, the SPP exhibits stochastic motion among the isotropic particles, always reaching the boundary of the confinement (Fig. 1c and Movie S1, ESI†). We note that, in contrast, an isotropic particle under the same conditions hardly moves from its initial position (see Fig. 6a). The virtual lack of diffusion indicates that the isotropic particles are in solid-like state *via* jamming, *i.e.*, they barely exchange positions among themselves. The jammed state, however, is disrupted by the SPP, which penetrates through the granular medium of isotropic particles. The trajectories of the SPP clearly indicate the significance of θ_L and the AR: the higher θ_L or AR tends to produce straighter trajectories, while the lower θ_L or AR creates more wiggly trajectories. Their quantitative effects are more evident in the time T for the SPP to reach the boundary, which decreases rapidly as θ_L or AR of the SPP is increased (Fig. 1d); an increase in θ_L or AR shortens the distance traveled to reach the boundary and increases the time-averaged velocity (see Fig. 7). These results are at odds with what one would naively expect from the velocity of an isolated SPP, which increases by at most 20% as θ_L is increased from 4° to 10° and barely changes with the AR (see Fig. 5). In other words, using the granular medium in the jammed state, the motion of the SPP becomes far more sensitive to its controllable physical attributes.

B. Superdiffusion of the self-propelled particle

To characterize the motion of the single SPP in more detail, we measured its time-averaged mean squared displacement (MSD), which is defined as

$$\left\langle \overline{\Delta \mathbf{r}(t)^2} \right\rangle \equiv \left\langle \frac{1}{T-t}\int_0^{T-t} \mathrm{d}t' |\mathbf{r}(t+t') - \mathbf{r}(t')|^2 \right\rangle. \quad (1)$$

Here $\mathbf{r}(t)$ denotes the location of the SPP at time $t \geq 0$, and $\langle \cdots \rangle$ represents the ensemble average over different samples. As shown in Fig. 1e (for the case $\theta_L = 10°$), the SPP exhibits superdiffusion $\left\langle \overline{\Delta \mathbf{r}(t)^2} \right\rangle \sim t^{\gamma}$ with $1 < \gamma < 2$ for a time interval up to the order of seconds, which eventually crosses over to the normal diffusion with $\gamma = 1$ as time goes on. The diffusion exponent γ increases as the AR is increased, which is consistent with the visual observation shown in Fig. 1c that the SPP with a larger AR tends to exhibit a straighter trajectory. Such superdiffusion indicates the presence of nontrivial long-range temporal correlations in the motion of the SPP. To gain more information, we also separately examined the time-averaged mean squared angular displacement

$$\left\langle \overline{\Delta \theta(t)^2} \right\rangle = \left\langle \frac{1}{T-t}\int_0^{T-t} \mathrm{d}t' [\theta(t'+t) - \theta(t')]^2 \right\rangle, \quad (2)$$

where $\theta(t)$ indicates the orientation of the self-propulsion force. As shown in the inset of Fig. 1e, the angular motion already exhibits normal diffusion on a subsecond time scale. This implies that the angular motion of the SPP is effectively an unbiased Brownian motion subject to a randomly fluctuating torque whose autocorrelation decays rapidly in time. On a time scale longer than the inverse of the angular diffusion coefficient, the orientation θ becomes fully randomized, and the position of the SPP starts to exhibit normal diffusion. It is also notable that the higher AR leads to the lower angular diffusion coefficient $D_r = \left\langle \overline{\Delta \theta(t)^2} \right\rangle \Big/ 2t$ in a dense granular media. As shown in the inset of Fig. 1e, D_r of an SPP with AR = 2 is about $10^{0.6} \approx 25\%$ of that of a circular SPP. One possible factor contributing to this decrease is the oscillation amplitude, which becomes slightly smaller when the AR is increased (see Fig. 8). However, for the case $\theta_L = 10°$ shown in Fig. 1e, the AR hardly affects D_r in the absence of the granular particles. Thus, the lower D_r for the higher AR in the granular medium is due to the angular motion of the elongated SPP being more strongly suppressed by the torque applied by the surrounding isotropic particles. Thanks to this effect, the SPP with a higher AR keeps its initial orientation for a longer time, traveling through a straighter route as shown in Fig. 1c.

Now we move on to the axial motion of the SPP. For this purpose, we examine the properties of the axial velocity and the axial displacement of the SPP, which are respectively defined as

$$v_{\parallel}(t) \equiv \dot{\mathbf{r}}(t) \cdot \hat{\mathbf{e}}_{\theta(t)}, \quad l_{\parallel}(t) \equiv \int_0^t \mathrm{d}t' v_{\parallel}(t'), \quad (3)$$

where $\hat{\mathbf{e}}_{\theta} \equiv (\cos\theta, \sin\theta)$ denotes the orientation of the self-propulsion force. By this definition, $l_{\parallel}$ increases (decreases) if the SPP travels in the direction of (against) its self-propulsion. As exemplified for AR = 1.0 by the inset of Fig. 1f, $l_{\parallel}$ rarely decreases in time but tends to increase *via* a series of steps alternating with plateaus of various lengths between adjacent pairs of steps. This indicates that the SPP is usually trapped by a cage composed of the surrounding particles but occasionally moves forward by cracking it.

To characterize such intermittent translation quantitatively, we measured the trapping time τ, here defined as the time it takes for $l_{\parallel}$ to increase by a step of 20 mm (the diameter of each isotropic particle). See the inset of Fig. 1f for an illustration, where the spacing between every adjacent pair of vertical blue lines corresponds to an instance of τ. Its distribution, as shown in the main figure, exhibits a broad power-law tail $P(\tau) \sim \tau^{-\alpha}$ with $2 < \alpha < 3$. Moreover, we also examined the power

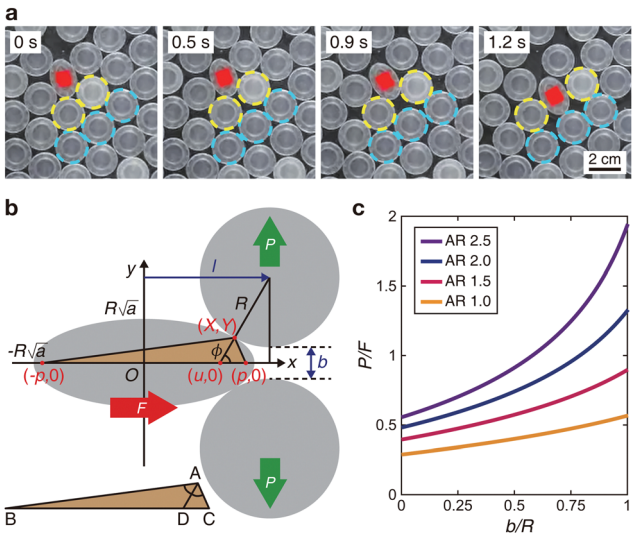

Fig. 2 Analysis of the effect of aspect ratio on cracking ability. (a) Images of a single SPP with AR = 1.5 (marked by a red tape) penetrating the gap between two isotropic particles (yellow dotted circles) in front. (b) Coordinate system for calculating the cracking force P that widens the gap b between two isotropic particles. (c) The relative magnitude of the cracking force P/F as b/R and AR are varied.

spectrum $S(f) = |\hat{v}_\parallel(f)|^2$ obtained from the Fourier transform of the axial velocity:

$$\hat{v}_\parallel(f) \equiv \int_0^T \mathrm{d}t v_\parallel(t) \mathrm{e}^{-2\pi i f t}. \tag{4}$$

As shown in Fig. 1g, the power spectrum exhibits a $1/f$ noise behavior $S(f) \sim f^{-\beta}$ with $0 < \beta < 1$, where the exponent β decreases with the AR. According to the inset of Fig. 1g, the two power-law exponents α and β satisfy the relation $\alpha + \beta = 3$ within the error bars. We stress that this relation between α and β is not a result of curve fitting, but an analytically proven[31] feature of the fractal renewal process, which consists of a series of delta-peak signals with a power-law interevent time distribution $P(\tau) \sim \tau^{-\alpha}$. Thus, the axial motion of the SPP can be described as a fractal renewal process composed of static states (caging) of power-law distributed durations punctuated by abrupt jumps of the same length (cracking). This reflects the quasi-long-range temporal correlations present in the axial motion, because of which the initial motion of the SPP is neither diffusive nor ballistic, but superdiffusive.

C. Effects of the particle shape on the cracking force

We see from the above analysis that α increases (β decreases) with the AR, which implies that a sharper SPP finds it easier to crack the cage. A step-by-step view of such cracking motion is shown in Fig. 2a, where the SPP (marked by a red tape) finds and widens a gap between a pair of neighboring isotropic particles highlighted in yellow dashed lines. To understand how a larger AR enhances the cracking motion, in the following we calculate the cracking force applied by the SPP that widens the gap between the two isotropic particles in front.

For simplicity, we assume that the system is at static mechanical equilibrium. Although this assumption is not strictly true in the actual experiment, the results obtained from this assumption still give us a useful picture of how the AR of the SPP affects the cracking dynamics. As shown in Fig. 2b, we consider the situation where an elliptic SPP of AR = a propels itself to the right by self-propulsion force F and pushes the neighboring isotropic particles of radius R by cracking force P. Here, ϕ is the angle between the x-axis and a line passing through the center of the adjacent circle and the point of contact (X,Y), and $(u,0)$ is the intersection between the line and the x-axis. We first use the properties of ellipses to represent the horizontal and vertical distances l and b in terms of just a and X. Using the coordinate system employed in Fig. 2b, the elliptic perimeter of the horizontal SPP centered at the origin is expressed by

$$\frac{x^2}{aR^2} + \frac{ay^2}{R^2} = 1, \tag{5}$$

which also includes the point of contact (X,Y). A useful property of the ellipse is that the triangle in Fig. 2b satisfies $\overline{\mathrm{AB}}:\overline{\mathrm{AC}} = \overline{\mathrm{BD}}:\overline{\mathrm{DC}}$, which implies

$$\frac{(X+p)^2 + Y^2}{(X-p)^2 + Y^2} = \frac{(p+u)^2}{(p-u)^2}. \tag{6}$$

From the geometry of the ellipse, the locations of its foci $(\pm p, 0)$ satisfy $p = R\sqrt{a - a^{-1}}$. Combining this relation with eqn (5) and (6) and choosing the suitable root of the quadratic equation, we obtain

$$u = X\left(1 - \frac{1}{a^2}\right). \tag{7}$$

This equation, along with eqn (5), allows us to express Y and u as functions of X and a.

We then consider the angle ϕ. From the two points, (X,Y) and $(u,0)$, $\sin\phi$ and $\cos\phi$ can be represented by $Y/[(X-u)^2 + Y^2]$ and $(X-u)/[(X-u)^2 + Y^2]$, respectively. Using eqn (5) and (7), we can relate the trigonometric functions to X and a by

$$\sin\phi = \frac{\sqrt{R^2/a - (X/a)^2}}{\sqrt{X^2/a^4 + R^2/a - (X/a)^2}}, \tag{8}$$

$$\cos\phi = \frac{X/a^2}{\sqrt{X^2/a^4 + R^2/a - (X/a)^2}}. \tag{9}$$

Substituting eqn (8) and (9) into $l = X + R\cos\phi$ and $b = 2(Y + R\sin\phi - R)$, the two distances l and b are represented as a function of a and X.

Now we express the cracking force P in terms of a and X. By the assumption of static mechanical equilibrium, the principle of virtual work[42] states that the cracking force P and the self-propulsion force F must satisfy the relation

$$F\delta l + 2P(\delta b/2) = 0, \tag{10}$$

where δl and δb are infinitesimal virtual displacements associated respectively with the horizontal and vertical distances l

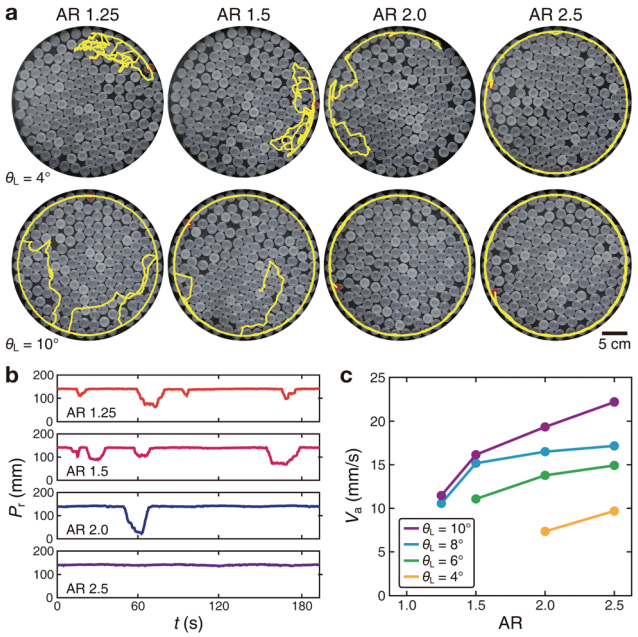

Fig. 3 Dynamics of a single SPP after reaching the boundary. (a) The SPP trajectories for 3 min after reaching the boundary as the leg tilt angle θ_L and the AR are varied (Movie S2, ESI†). (b) The time evolution of the radial position P_r of the SPP at $\theta_L = 8°$. (c) The time-averaged velocity V_a of the SPP moving along the boundary. The quantity is calculated only for particles moving on the boundary for 30 s without stopping or leaving the boundary.

and b. Note that the second term on the left-hand side of the above equation accounts for the virtual work on both upper and lower isotropic particles. Using this relation, the cracking force is obtained as

$$P = -F\frac{\mathrm{d}l}{\mathrm{d}b} = -F\frac{\mathrm{d}l/\mathrm{d}X}{\mathrm{d}b/\mathrm{d}X}, \tag{11}$$

where X is the horizontal coordinate of the point of contact between the SPP and either of the isotropic particles. Substituting $l = X + R\cos\phi$ and $b = 2(Y + R\sin\phi - R)$ along with eqn (8) and (9) in eqn (11), we finally obtain the curves shown in Fig. 2c.

The behavior of P as a function of the AR and the gap b is shown in Fig. 2c. It shows that P monotonically increases with the AR; at $b = 0$, the magnitude of P applied by an SPP with AR = 2.5 is about twice as large as that exerted by the circular SPP. This ratio increases even more as b increases. We also note that P is smaller for a narrower gap (smaller b), which indicates that cracking becomes harder in more crowded environments. These results confirm our observation that the shape of the SPP greatly affects its mobility within a dense granular medium *via* the rotational and cracking characteristics.

D. Boundary motion of the self-propelled particle

Finally, we briefly discuss how the SPP moves after reaching the confinement boundary. Using our setting, if there is no SPP, an isotropic particle initially located at the boundary stays there while exhibiting some diffusion only in the tangential direction (see Fig. 6b). This again confirms that the granular system satisfies the jamming condition, *i.e.*, the relative positions of the particles do not change, although the entire cluster may exhibit rotational diffusion. In contrast, as shown in Fig. 3a, the SPP reaching the boundary exhibits a high mobility through the granular medium. The SPP tends to stay close to the boundary, as expected for a particle whose direction of motion exhibits a degree of persistence.[43] But how close to the boundary the SPP stays depends on the AR and θ_L. Since the cracking ability and the orientational persistence of the SPP both increase with the AR, the SPP with a higher AR tends to stay closer to the boundary (Fig. 3a, b, Movie S2, ESI†) with a higher velocity V_a tangential to the boundary (Fig. 3c). In addition, since the self-propulsion force monotonically increases with θ_L below 10°, the SPP tends to move faster along the boundary as θ_L is increased. We also note that the SPP deviates farther away from the boundary at higher AR, albeit at a reduced frequency (see Fig. 3b). This behavior is also attributable to the enhanced cracking ability and the orientational persistence of the SPP with a higher AR.

IV. Motion of multiple self-propelled particles at the boundary

A. Formation of the boundary cluster

As previously mentioned, when the AR is high enough, an individual SPP in the vibrated granular medium moves to the boundary and travels along it in a unidirectional manner. With this in mind, now we examine the collective behavior of multiple SPPs in a granular medium confined by a circular boundary. We place multiple SPPs with AR = 2.5 and $\theta_L = 10°$ in the bulk of the previously described experimental system, with each SPP replacing a single isotropic particle so that the packing fraction stays at 75% as in the single-SPP experiments. When the vibration is turned on, as shown in Fig. 4a (for $t < 40$ s), all the SPPs move from the bulk to the boundary, and then they collide with each other at the boundary. When they collide while moving in the opposite directions along the boundary, either they simply pass by, or one of them leaves the boundary and returns to the bulk (see Fig. 9a and b). On the other hand, if they collide while moving in the same direction along the boundary, they tend to stay close to each other and keep their original traveling direction even after the collision (see Fig. 9c). These imply that only a cluster of SPPs that used to travel in the same direction can form a stable structure, acting as the attractor of the collective dynamics of the SPPs. Indeed, our experiments show that the SPPs gradually merge into one large cluster (Fig. 4a, 40 s $< t <$ 80 s) and travel together along the boundary (Fig. 4a, $t >$ 80 s).

B. Motility of the boundary cluster

It is worthwhile to examine in more detail how a cluster of SPPs can persistently travel in a single direction along the boundary. In Fig. 4a, for $t >$ 80 s, we observe that all the SPPs forming a cluster are tilted from the radial direction in an asymmetric manner. For example, the rearmost SPP, indicated by a yellow

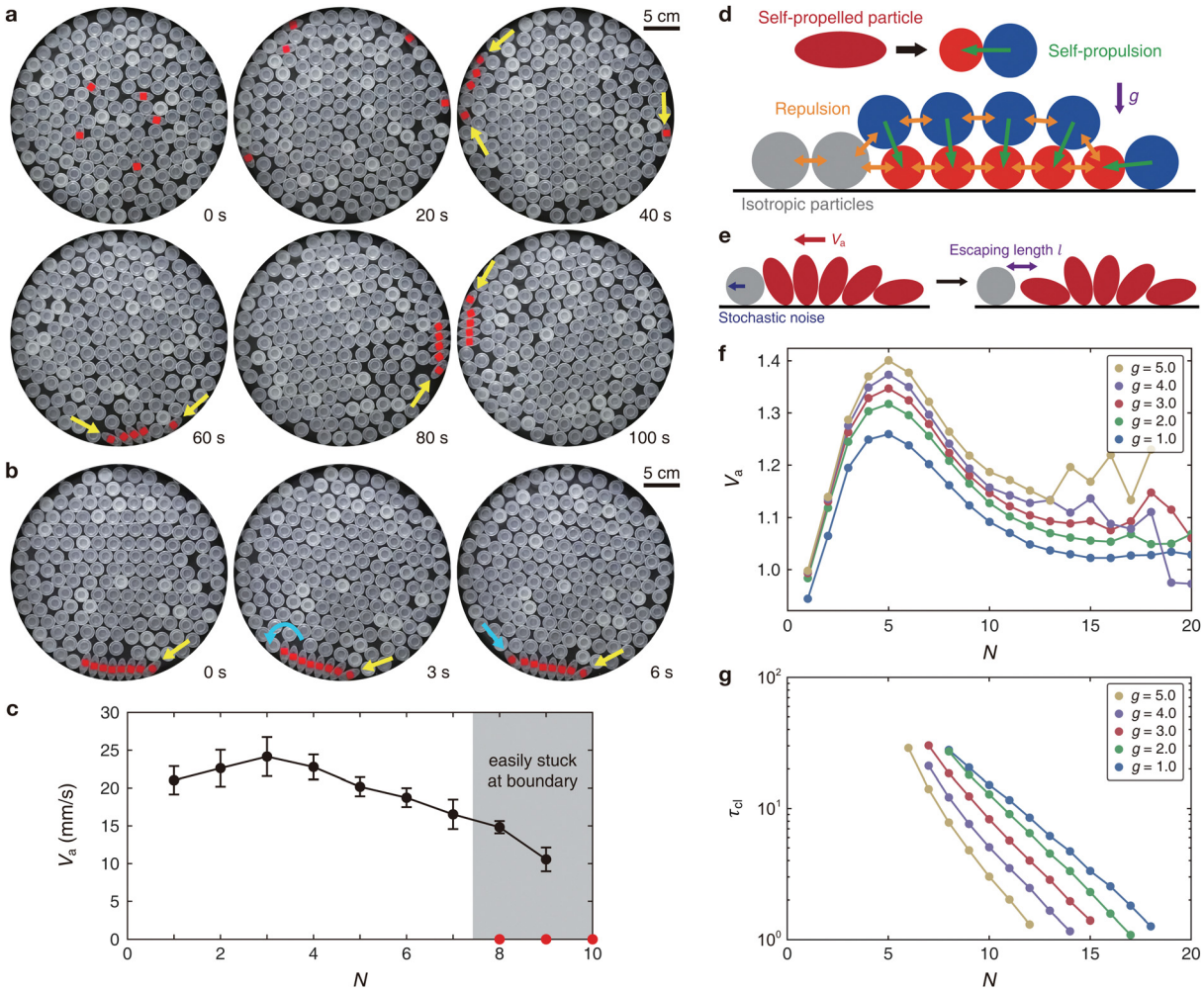

Fig. 4 Collective motion of multiple SPPs. (a) Five SPPs, initially located in the bulk, reach the boundary and form a cluster that persistently maintains its asymmetric structure and mobility in a single direction (Movie S3, ESI†). (b) A moving cluster of eight SPPs gets stuck after the leading SPP switches its direction and restores the symmetry. (c) The time-averaged velocity V_a of the SPP cluster as the number N of the SPPs varies (Movie S4, ESI†). The velocity is calculated from the SPP cluster moving persistently in one direction for more than 2 min. Meanwhile, the red points indicate that the SPP clusters with $N > 7$ mostly stay stuck at the boundary after 5 min of observation time. Error bars indicate standard deviation. All SPPs in (a)–(c) have AR = 2.5 and θ_L = 10°. (d) An illustration of our simplified model of the SPP cluster dynamics. The effective outward force applied by the bulk granular particles is indicated by g. (e) An illustration of the effective process by which the moving SPP cluster gets stuck. (f) and (g) The magnitude of V_a (f) and the mean lifetime τ_{cl} (g) of the moving SPP cluster as N and g vary.

arrow, exhibits a significant tilt that makes it almost completely lean against the confinement boundary. In contrast, the frontmost SPP tends to tilt only slightly, usually leaning against an isotropic particle in front. Thus, whereas the rearmost SPP strongly pushes the cluster forward, the frontmost SPP provides only a weak resistance to the cluster motion. The cluster moves forward as a result of this force imbalance, which makes the isotropic particle in front of the cluster to stick more strongly to the frontmost SPP. Thus, despite the microscopic noise, the frontmost SPP maintains a limited tilt, keeping the asymmetric arrangement of the SPPs in the cluster. In short, there is a positive feedback between the structural asymmetry and the motility of the SPP cluster, which allows it to maintain a persistent motion *via* spontaneous symmetry breaking. This state of motion may be called the moving phase.

However, the above mechanism fails to maintain the motion of the SPP cluster when the number N of SPPs is too large. The case of $N = 8$ is illustrated in Fig. 4b. For $0 < t < 3$ s, the cluster maintains its motion according to the positive feedback mechanism described above. However, at approximately $t = 3$ s, the isotropic particle in front of the cluster happens to move sufficiently far away from the frontmost SPP. This allows the frontmost SPP to lean completely against the boundary, leading to both the rearmost and the frontmost SPPs exerting about the same magnitude of force on the SPP cluster in opposite directions. Thus the SPP cluster assumes a symmetric structure and loses its persistent mobility. This state of motion may be called the static phase.

How does N affect the phase of the SPP cluster, and what is the nature of the transition between the moving phase and the static phase? As shown in Fig. 4c, the time-averaged velocity V_a

of the SPP cluster tends to decrease as N is increased (with a notable exception created by a maximum V_a attained at $N = 3$, which will be discussed later), with multiple metastable values observed for $N > 7$. To put it more precisely, for $N > 7$, the SPP cluster may exhibit a prolonged period of persistent motion, which eventually comes to a halt as the frontmost particle flips over to restore the cluster symmetry according to the mechanism described above. After that, the cluster is stuck, never resuming motion within the observation time. These results, especially the coexistence of multiple metastable states of motion for a range of N, indicate that the transition between the moving and the static phases is discontinuous. This is also corroborated by the results shown in Fig. 10, where the moving phase and the static phase seem to coexist for $N \geq 7$, with the static phase becoming more likely than the moving phase as N increases from 7 to 8.

C. Simple model of cluster motility

Due to difficulties in increasing the number of samples and the observation time, we could not reliably estimate the stability of the moving SPP cluster as the number of SPPs, N, was increased, which is crucial for understanding the nature of the phases and the transition between them. To circumvent the difficulty, we consider a simplified model of the SPP cluster as shown in Fig. 4d. The model assumes that a one-dimensional ring is filled with a total of N_{tot} particles, where a series of $N_{iso} \equiv N_{tot} - N$ isotropic particles (grey disks) are followed by a series of N SPPs (red-blue rigid dimers) that propel themselves along the axial directions (green arrows). To represent the boundary accumulation of the particles, we assume that all grey and red disks stay in contact with the boundary, while the blue disks are allowed to move in two dimensions to model the flipping behavior of the SPPs. Noting that the outward pressure resulting from the random short-range movement of bulk granular matter tends to make the SPPs lean against the boundary, the effect is implemented by introducing an effective gravity g into the dynamics. Every pair of particles interacts *via* the Weeks–Chandler–Andersen (WCA) potential (orange arrows), and the microscopic noise originating from the plate vibration is modeled by the Gaussian white noise. See the Methods for more detailed description of the model. As Fig. 4d schematically shows, this model also exhibits persistent motion of the SPP cluster maintained by a symmetry-breaking mechanism very similar to the one observed in the experiment. Moreover, as illustrated in Fig. 4e, the cluster mobility is eventually lost when the isotropic particle (grey disk) in front of the traveling cluster (red elliptic disks) moves sufficiently far away from the frontmost SPP, allowing it to lean against the boundary.

We first observe how the time-averaged velocity V_a of the cluster changes depending on the number N of SPPs for different magnitudes of the gravity g. As shown in Fig. 4f, the model reproduces the existence of an optimal number of SPPs that maximizes the cluster velocity. This effect seems to be caused by the geometric shape of the SPPs. When N is small, each additional SPP means one more pusher and one less isotropic particle in front to be pushed, so V_a increases with N. But when N is increased further, the elliptic shape of each SPP (narrower at the tip, fatter in the center) means that the SPPs farther away from the rear tends to tilt more and more against the motion of the cluster. When this happens, an additional SPP means an active obstacle pushing against the moving cluster in place of a passive obstacle simply staying in front. Thus, V_a would eventually start to decrease when N goes above a certain threshold, which may be regarded as the "optimal" N. If the boundary shown in Fig. 4d bends upward (due to a finite radius of curvature), the optimal N would become smaller. This explains why the optimal N in the experiment (found to be 3 in Fig. 4c) is smaller than that found in our simplified model (found to be 5 in Fig. 4f). We also see that the increase in g, which tilts the SPPs more toward the boundary, makes the cluster move faster along the boundary.

Next, we turn to the question of how a large SPP cluster switches from a moving state to a static state. As schematically illustrated in Fig. 4e, for a moving cluster to be stuck, the $N_{iso} = N_{tot} - N$ isotropic disks in front should move sufficiently far away from the frontmost SPP of the cluster by the length l of the SPP, so that the SPP can fully lean against the boundary. This is like overcoming an effective potential barrier

$$\Delta E \sim (N_{tot} - N) l V_a / \mu_m \quad (12)$$

arising from the fictitious force V_a/μ_m in the cluster frame of reference, where μ_m is the mobility coefficient. Assuming that the noise is analogous to that of an equilibrium system characterized by some effective temperature T_{eff}, the Arrhenius' law governing the mean escape time from a potential well states that the SPP cluster maintains its unidirectional motion over a time scale

$$\tau_{cl} \sim \exp[\Delta E / T_{eff}] \sim \exp[-N \times \text{constant}]. \quad (13)$$

For this reason, the lifetime of the moving cluster decays exponentially with the number of SPPs N, as shown in Fig. 4g.

Although not implemented in our simplified model, a static, symmetric cluster of SPPs can be turned into a mobile, asymmetric cluster when the leftmost/rightmost SPP is kicked up *via* collision with the adjacent granular particle, inducing the cluster asymmetry. The time scale of this happening will not depend appreciably upon the number N of SPPs since it only concerns the two SPPs at both ends of the cluster. Thus, while the rate of a static cluster becoming mobile changes insignificantly with N, the rate of a moving cluster becoming static increases exponentially with N. For this reason, when N crosses a certain threshold, the relative stability of the moving phase and the static phase will change dramatically, leading to a phase coexistence behavior indicating a discontinuous transition.

V. Conclusions

We have presented experimental and numerical results that show how the easily tunable attributes of the SPPs, such as their AR and number, significantly change their individual and collective dynamics in a vibrated dense granular medium. Here

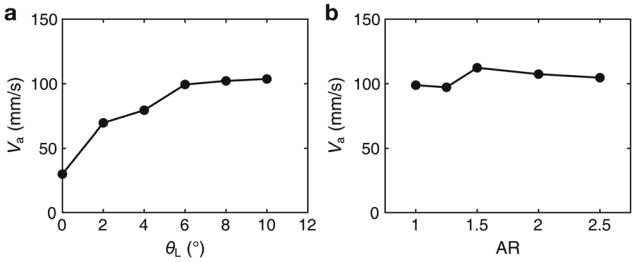

Fig. 5 The average axial velocity of a single SPP without any surrounding particles. (a) The time-averaged velocity V_a as a function of the leg tilt angle θ_L when AR = 1. (b) V_a as a function of AR when $\theta_L = 10^\circ$.

follow comparisons between our findings and the notable results reported in the literature.

In the absence of the granular medium, the motion of the single SPP on the vibrating plate can be faithfully described as the active Brownian motion with largely constant axial velocity and weak rotational diffusion, as already reported in previous studies.[16,17] The velocity and the rotational diffusion coefficient of the SPP do not exhibit a strong dependence on its AR, especially when the self-propulsion is sufficiently strong ($\theta_L = 10^\circ$) (see Fig. 5 and 8). But, when surrounded by a dense granular medium of isotropic particles, we observed that the AR strongly affects both axial and rotational components of the SPP motion *via* cage formation and cracking. For this reason, the easily tunable microscopic attributes of the SPPs have far greater impact on the self-organization process in the presence of the dense granular medium than in its absence.

Previous studies also reported that a large number of SPPs, *via* direct mechanical interactions[16,17] or indirect interactions mediated by the granular medium,[28] develop a long-range orientational order. This phenomenon, called flocking, requires that the confining boundary of the system be designed so that the SPPs sticking to the boundary are constantly guided back into the bulk.[16,17,28] Without such boundary, the SPPs eventually form a static cluster that sticks to the boundary and hardly move as a whole, preventing the formation of a flock. This precisely corresponds to the static boundary cluster for large N discussed in Section IV. Since these studies focused only on a system consisting of a macroscopically large number of SPPs, they missed the possibility of a small number of SPPs forming a motile cluster whose polarity and cohesion are maintained by the surrounding dense granular medium.

Our findings pave the way for a variety of interesting future investigations. First, the precise relation between the self-organized structure of the SPPs and the physical properties of the surrounding granular medium is yet to be clarified. While the enhanced effects of the SPP's shape on its dynamics and the formation of the traveling cluster at the boundary do seem to require the presence of caging, we still need to examine how these phenomena change depending on various characteristic time and length scales of the granular medium as its packing fraction and vibration protocols are varied. A related issue is how the presence of granular materials affects the boundary accumulation of the SPPs, which still occurs even without the granular materials.[44,45] It would be interesting to check if local variations in the vibration protocols can allow us to control the form of the self-organized structure in a manner similar to the light-induced patterns formed by swimming bacteria.[46] Second, we may explore the self-organization behaviors of the system for a flexible confinement boundary. We expect such systems to exhibit a rich range of collective dynamics *via* feedback between SPP ordering and membrane deformation. Their behaviors may also give us some clues as to the dynamical properties of cells and vesicles, which are by themselves crowded systems consisting of SPPs enclosed by flexible membranes. Finally, we also need to investigate whether our findings generalize to the case where the particles are even softer and thus highly deformable. This may give us a physical picture of how highly motile and invasive cells spread amidst a confluent tissue of epithelial cells, with ramifications for the mechanisms of morphogenesis and cancer metastasis.[47]

Author contributions

K. S., Y. B. and H.-Y. K. designed research and wrote the paper. K. S. performed experiments and analyzed experimental data. K. S. Y. C., E. K., L. G. R., and Y. B. performed theoretical analysis.

Conflicts of interest

Authors declare no competing interest.

Appendices

Appendix A: simulation details for the simple model of the SPP cluster

We consider a 2D system consisting of $N_{tot} = 25$ particles in total. N of them are rigid dimers (SPPs) that propel themselves along their axes, while the rest are isotropic particles without any self-propulsion (Fig. 4d). Each isotropic particle is a (grey) disk of radius $a_1 = 6$. Each dimer consists of a smaller (red) disk of radius $a_2 = 4$ and a larger (blue) disk of radius $a_3 = 4.6$ separated by a fixed distance $l = 4$, so that the overall envelope of the dimer imitates the elliptic particle used in our experiments. The smaller (larger) particle corresponds to the front (rear) of the SPP, and the self-propulsion force $F = 100$ (green arrow) always acts from the center of the larger particle towards that of the smaller particle. Assuming that each SPP always stays in contact with the boundary, we constrain all isotropic (gray) particles and the smaller (red) particles of the dimers to move along the 1D periodic line, which is a zero-curvature simplification of the circular confinement boundary used in our experiments. The length of the periodic line is set to be

$$L = 2a_1(N_{tot} - N) + 2a_2(N - 1) + (a_2 + a_3 + l), \quad \text{(A1)}$$

which is roughly equal to the total length occupied by the particles, provided that all but one SPP stand vertically and the remaining SPP leans completely against the boundary. In other

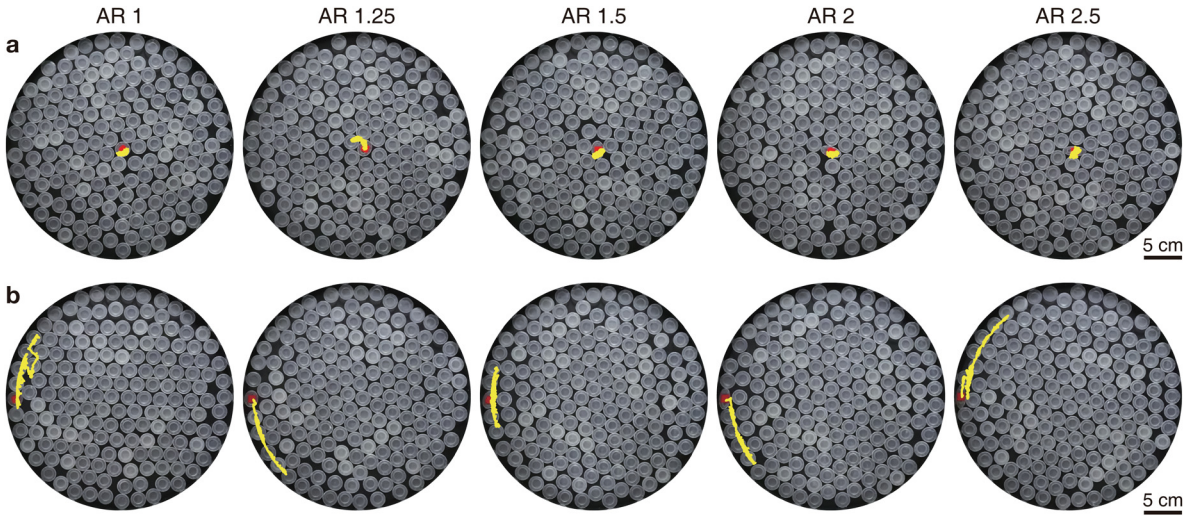

Fig. 6 Trajectories of a single isotropic particle placed amidst a crowd of isotropic particles. The particle's position is tracked for 3 minutes starting from the initial position at (a) the center and (b) the boundary of the confinement as the AR is varied.

words, this setting ensures that the system is densely packed with the packing fraction close to unity.

Now we describe three types tof forces (other than the self-propulsion F) acting on each of the particles. First, given the distance r_{ij} between particles i and j, their short-range repulsion is given by the gradient of the Weeks–Chandler–Andersen (WCA) potential

$$U(r_{ij}) = \begin{cases} 4\varepsilon\left[\left(\frac{\sigma_{ij}}{r_{ij}}\right)^{12} - \left(\frac{\sigma_{ij}}{r_{ij}}\right)^{6}\right] + \varepsilon & \text{if } r \le 2^{1/6}\sigma, \\ 0 & \text{if } r > 2^{1/6}\sigma, \end{cases} \quad \text{(A2)}$$

where ε and σ_{ij} are respectively characteristic energy and distance parameters. The latter parameter is the sum of the respective radii a_i and a_j of particles i and j. The interactions arising from this potential are indicated by orange arrows in Fig. 4d. Second, there are random microscopic forces ultimately originating from the plate vibrations. While these forces have a characteristic driving frequency in the original experiment, here we represent them by a Gaussian white noise, simply focusing on the destabilizing effects of microscopic fluctuations. We put the diffusion coefficient associated with the noise equal to 4. Finally, we introduce a vertical gravitational force g

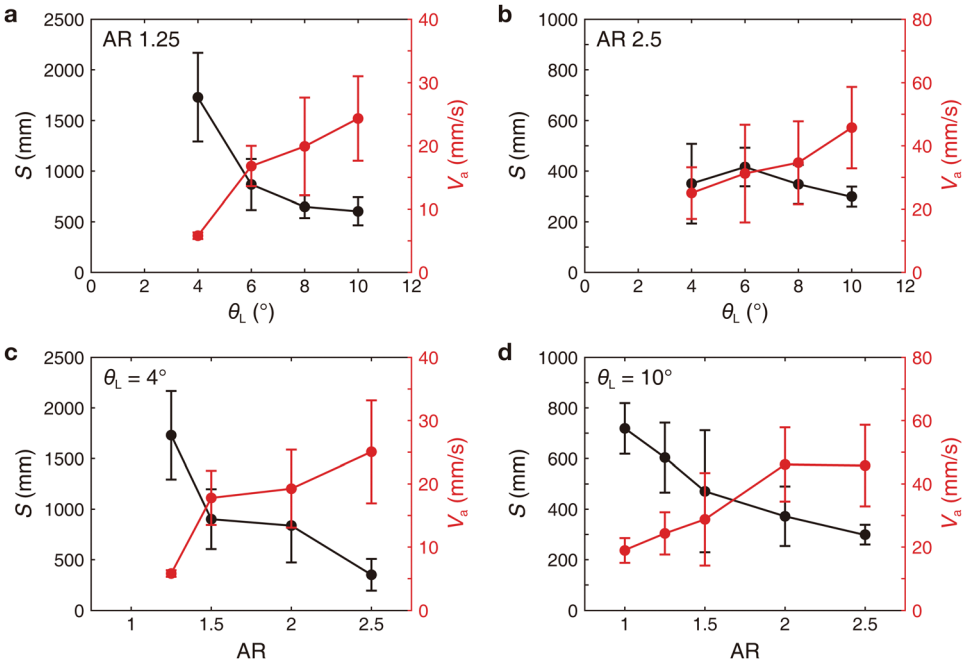

Fig. 7 Traveled distance and the time-averaged velocity of a single SPP in granular media from the center to the boundary. Results for different combinations of the AR and the leg tilt angle θ_L are shown. Error bars indicate standard deviation.

into the model, which corresponds to the outward pressure applied by the bulk granular medium that tends to make the SPPs lean against the boundary.

Implementing all the above elements, and assuming every particle to be overdamped with a mobility coefficient $\mu_m = 4$, their dynamics are numerically integrated using the Euler method.

Appendix B: supplemental figures

When the mass of the particle is fixed, the SPP's leg tilt angle θ_L and AR are main factors that affect its behavior. Fig. 5 shows the change in average velocity of a single SPP as a result of increasing θ_L and the AR when its movement is unimpeded by its surroundings. The axial velocity of the SPP increases with θ_L but converges as it approaches 10° (Fig. 5a), while it does not vary significantly with the AR (Fig. 5b). This indicates that the SPP's self-propulsion is only affected by θ_L, and the influence decreases as θ_L increases.

Fig. 6 shows how particle move when only isotropic particles without SPP densely fill the circular arena. An isotropic particle located at the center can hardly exchange its position with other particles except by slight oscillation (Fig. 6a). For a particle situated at the boundary, it remains stationary, undergoing diffusion exclusively in the tangential direction (Fig. 6b). This affirms that isotropic particles are in a jammed state, even though the entire cluster may display rotational diffusion.

Fig. 7 shows the effect of θ_L and AR on the time-averaged speed V_a and distance S traveled by a single SPP from the center of a dense environment to the boundary. At low AR, a rise in θ_L leads to both an increase in V_a and a decrease in S (Fig. 7a). However, at high AR, x causes a significant change in V_a only (Fig. 7b). On the other hand, an increase in AR significantly increases V_a and decreases S for both low and high θ_L (Fig. 7c and d). This indicates that the SPP's AR has a considerable impact on both its ability to penetrate and redirect in a dense environment.

The θ_L and AR of the particle also affect its rotational properties. Fig. 8a shows that increasing both variables generally suppresses the rotational movement of the SPP. The cause of this effect can be found in Fig. 8b–d, which show that an increase in the two variables inhibits the particle's vertical movement generated by the vibrating plate. Increasing θ_L diminishes the vertical deformation of the particle legs, while elongating particles enhances the likelihood of certain legs adhering to the bottom plate. This impedes the rotation of the particle, a phenomenon primarily observed when the particle falls off the floor.

Fig. 9a and b shows how two SPPs moving in opposite directions at a boundary behave after a collision. Typically, they either traverse along the boundary without significant changes or, alternatively, one of them exits the boundary. The particle that returns to the bulk will eventually encounter the boundary again, and this process continues until they move in the same direction along the boundary. Unless the two particles are moving at precisely the same speed, they will eventually meet at a certain point. Subsequently, they will coalesce into a

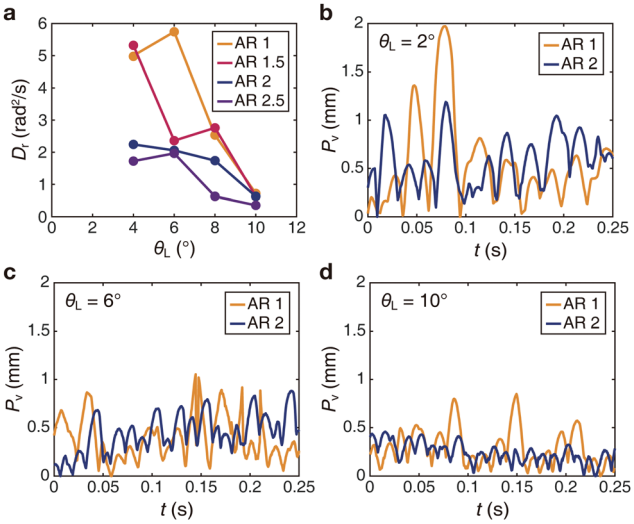

Fig. 8 Rotational and vibrational properties of a single isolated SPP. (a) Rotational diffusion coefficient D_r tends to decrease with the increasing AR and the increasing leg tilt angle θ_L. (b)–(d) Change of the vertical position P_v of the SPP as the AR and the leg tilt angle θ_L are varied.

cluster and continue their motion in the original direction (Fig. 9c).

Fig. 10 depicts a time-dependent histogram of SPP cluster velocities along the boundary for each cluster size, initially exhibiting motion in a single direction. When N is 3 or less, all clusters maintain their initial direction, but as SPP is added, several clusters appear to switch their orientation. In particular, from $N \geq 8$, many clusters switch from moving phase to static phase, and when $N = 9$, almost all clusters get stuck to the wall over time. The rise in the quantity of stationary clusters over

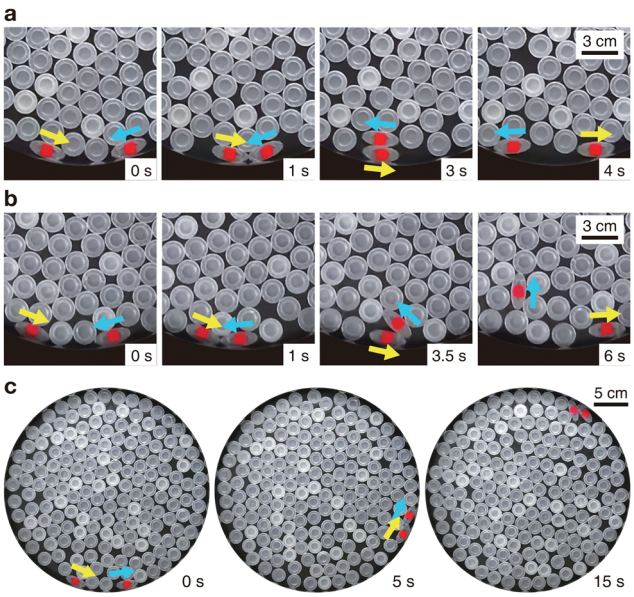

Fig. 9 Collisions between two SPPs at the boundary. A pair of SPPs traveling in the opposite directions may (a) pass each other or (b) get scattered into the bulk. Meanwhile, (c) two SPPs moving in the same direction tends to form a cluster.

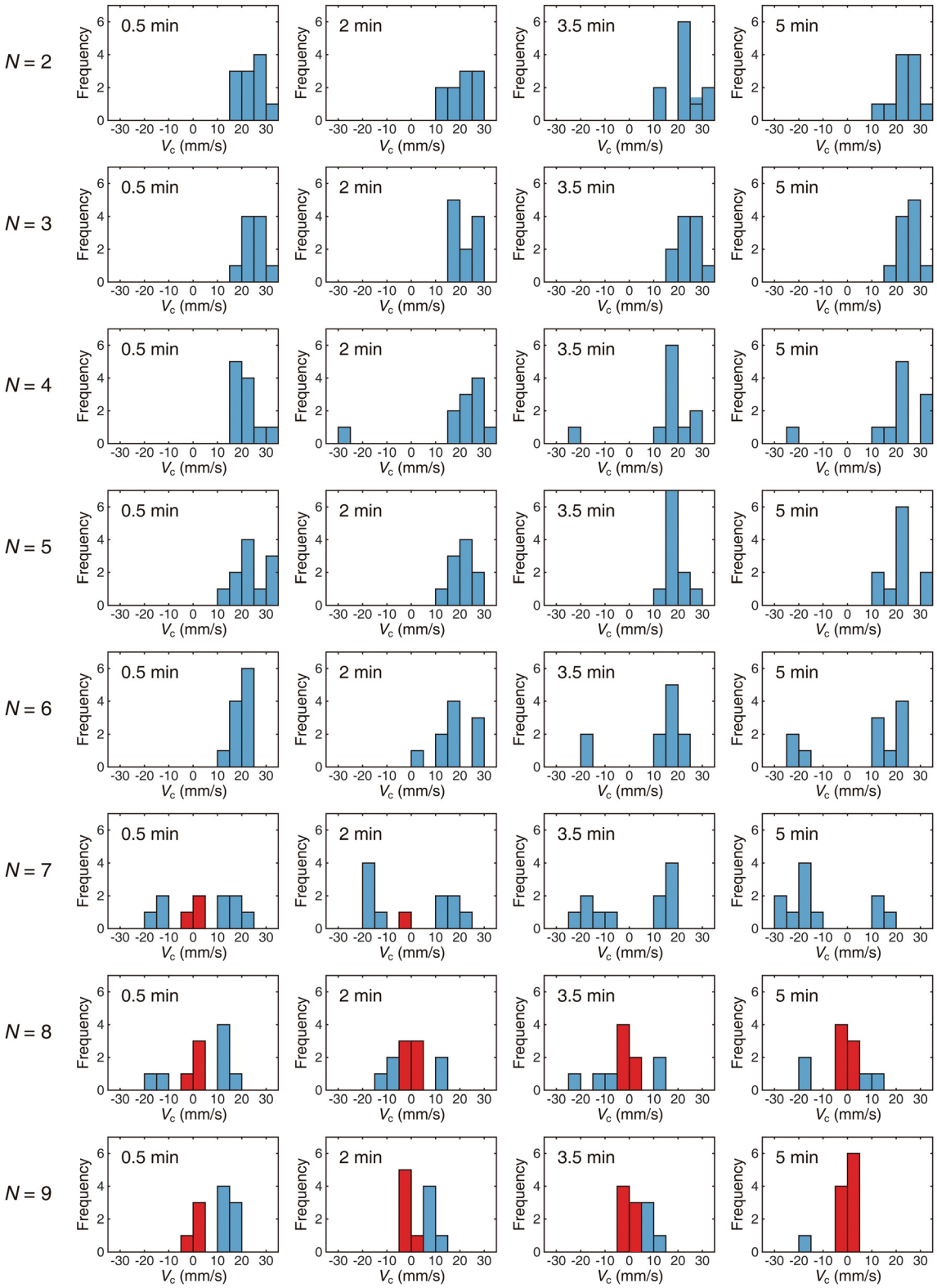

Fig. 10 Time evolution of the distribution of the short-term cluster velocity V_c. The quantity is measured for 5 s before and after each indicated time stamp. The red bars correspond to the static phase.

time implies that once a large cluster transitions into a static phase, it faces difficulties returning to a moving phase.

Acknowledgements

This work was supported by the National Research Foundation of Korea (Grant no. 2018-052541, 2021-017476) *via* SNU SOFT Foundry Institute. We acknowledge an administrative support from SNU Institute of Engineering Research.

References

1 S. Camazine, J.-L. Deneubourg, N. R. Franks, J. Sneyd, G. Theraula and E. Bonabeau, *Self-Organization in Biological Systems*, Princeton University Press, 2003.
2 M. Brambilla, E. Ferrante, M. Birattari and M. Dorigo, *Swarm Intell.*, 2013, **7**, 1–41.
3 M. Rubenstein, A. Cornejo and R. Nagpal, *Science*, 2014, **345**, 795–799.
4 L. Cademartiri and K. J. M. Bishop, *Nat. Mater.*, 2014, **14**, 2–9.
5 X. Tang, B. Rupp, Y. Yang, T. D. Edwards, M. A. Grover and M. A. Bevan, *ACS Nano*, 2016, **10**, 6791–6798.
6 W. Wang, J. Giltinan, S. Zakharchenko and M. Sitti, *Sci. Adv.*, 2017, **3**, e1602522.
7 I. Slavkov, D. Carrillo-Zapata, N. Carranza, X. Diego, F. Jansson, J. Kaandorp, S. Hauert and J. Sharpe, *Sci. Rob.*, 2018, **3**, eaau9178.
8 U. Culha, Z. S. Davidson, M. Mastrangeli and M. Sitti, *Proc. Natl. Acad. Sci. U. S. A.*, 2020, **117**, 11306–11313.
9 A. J. Rader, B. M. Hespenheide, L. A. Kuhn and M. F. Thorpe, *Proc. Natl. Acad. Sci. U. S. A.*, 2002, **99**, 3540–3545.
10 M. V. Chubynsky, M.-A. Briére and N. Mousseau, *Phys. Rev. E: Stat., Nonlinear, Soft Matter Phys.*, 2006, **74**, 016116.
11 H. M. Jaeger, S. R. Nagel and R. P. Behringer, *Rev. Mod. Phys.*, 1996, **68**, 1259–1273.
12 A. J. Liu and S. R. Nagel, *Nature*, 1998, **396**, 21–22.
13 I. S. Aranson and L. S. Tsimring, *Rev. Mod. Phys.*, 2006, **78**, 641–692.
14 B. Andreotti, Y. Forterre and O. Pouliquen, *Granular Media: Between Fluid and Solid*, Cambridge University Press, 2013.
15 P. Melby, F. V. Reyes, A. Prevost, R. Robertson, P. Kumar, D. A. Egolf and J. S. Urbach, *J. Phys.: Condens. Matter*, 2005, **17**, S2689.
16 J. Deseigne, O. Dauchot and H. Chaté, *Phys. Rev. Lett.*, 2010, **105**, 098001.
17 J. Deseigne, S. Leonard, O. Dauchot and H. Chaté, *Soft Matter*, 2012, **8**, 5629–5639.
18 C. A. Weber, T. Hanke, J. Deseigne, S. Léonard, O. Dauchot, E. Frey and H. Chaté, *Phys. Rev. Lett.*, 2013, **110**, 208001.
19 G. A. Patterson, P. I. Fierens, F. S. Jimka, P. G. König, A. Garcimartín, I. Zuriguel, L. A. Pugnaloni and D. R. Parisi, *Phys. Rev. Lett.*, 2017, **119**, 248301.
20 L. Caprini, F. Cecconi, C. Maggi and U. M. B. Marconi, *Phys. Rev. Res.*, 2020, **2**, 043359.
21 C. Reichhardt and C. J. O. Reichhardt, *Phys. Rev. E*, 2021, **103**, 062603.
22 G. Briand, M. Schindler and O. Dauchot, *Phys. Rev. Lett.*, 2018, **120**, 208001.
23 C. Scholz, M. Engel and T. Pöschel, *Nat. Commun.*, 2018, **9**, 931.
24 C. Scholz, A. Ldov, T. Pöschel, M. Engel and H. Löwen, *Sci. Adv.*, 2021, **7**, eabf8998.
25 R. Ni, M. A. Cohen Stuart and M. Dijkstra, *Nat. Commun.*, 2013, **4**, 2704.
26 R. Ni, M. A. Cohen Stuart, M. Dijkstra and P. G. Bolhuis, *Soft Matter*, 2014, **10**, 6609–6613.
27 B. Van Der Meer, L. Filion and M. Dijkstra, *Soft Matter*, 2016, **12**, 3406–3411.
28 N. Kumar, H. Soni, S. Ramaswamy and A. K. Sood, *Nat. Commun.*, 2014, **5**, 4688.
29 H. Soni, N. Kumar, J. Nambisan, R. K. Gupta, A. K. Sood and S. Ramaswamy, *Soft Matter*, 2020, **16**, 7210–7221.
30 N. Kumar, H. Soni, S. Ramaswamy and A. K. Sood, *Phys. Rev. E: Stat., Nonlinear, Soft Matter Phys.*, 2015, **91**, 030102.
31 S. B. Lowen and M. C. Teich, *Phys. Rev. E: Stat. Phys., Plasmas, Fluids, Relat. Interdiscip. Top.*, 1993, **47**, 992.
32 E. Tjhung, D. Marenduzzo and M. E. Cates, *Proc. Natl. Acad. Sci. U. S. A.*, 2012, **109**, 12381–12386.
33 G. De Magistris, A. Tiribocchi, C. A. Whitfield, R. J. Hawkins, M. E. Cates and D. Marenduzzo, *Soft Matter*, 2014, **10**, 7826–7837.
34 N. Nikola, A. P. Solon, Y. Kafri, M. Kardar, J. Tailleur and R. Voituriez, *Phys. Rev. Lett.*, 2016, **117**, 098001.
35 M. Shafiei Aporvari, M. Utkur, E. U. Saritas, G. Volpe and J. Stenhammar, *Soft Matter*, 2020, **16**, 5609–5614.
36 J. Howard, *Annu. Rev. Biophys.*, 2009, **38**, 217–234.
37 G. Foffano, J. S. Lintuvuori, K. Stratford, M. E. Cates and D. Marenduzzo, *Phys. Rev. Lett.*, 2012, **109**, 028103.
38 O. Granek, Y. Kafri and J. Tailleur, *Phys. Rev. Lett.*, 2022, **129**, 038001.
39 K.-W. Kim, Y. Choe and Y. Baek, *Phys. Rev. E*, 2024, **109**, 014614.
40 A. Kudrolli, G. Lumay, D. Volfson and L. S. Tsimring, *Phys. Rev. Lett.*, 2008, **100**, 058001.
41 J.-Y. Tinevez, N. Perry, J. Schindelin, G. M. Hoopes, G. D. Reynolds, E. Laplantine, S. Y. Bednarek, S. L. Shorte and K. W. Eliceiri, *Methods*, 2017, **115**, 80–90.
42 C. Lanczos, *The Variational Principles of Mechanics*, Dover, Toronto, 4th edn, 1986.
43 G. Li and J. X. Tang, *Phys. Rev. Lett.*, 2009, **103**, 078101.
44 L. Caprini and U. M. B. Marconi, *Soft Matter*, 2018, **14**, 9044–9054.
45 M. Leoni, M. Paoluzzi, S. Eldeen, A. Estrada, L. Nguyen, M. Alexandrescu, K. Sherb and W. W. Ahmed, *Phys. Rev. Res.*, 2020, **2**, 043299.
46 G. Frangipane, D. Dell'Arciprete, S. Petracchini, C. Maggi, F. Saglimbeni, S. Bianchi, G. Vizsnyiczai, M. L. Bernardini and R. Di Leonardo, *eLife*, 2018, **7**, e36608.
47 S. Grosser, J. Lippoldt, L. Oswald, M. Merkel, D. M. Sussman, F. Renner, P. Gottheil, E. W. Morawetz, T. Fuhs, X. Xie, S. Pawlizak, A. W. Fritsch, B. Wolf, L.-C. Horn, S. Briest, B. Aktas, M. L. Manning and J. A. Käs, *Phys. Rev. X*, 2021, **11**, 011033.

